

Distinctive 21 cm Structures of the First Stars, Galaxies, and Quasars

Hidenobu Yajima^{1*} and Yuexing Li^{2,3}

¹ *SUPA†, Institute for Astronomy, University of Edinburgh, Royal Observatory, Edinburgh, EH9 3HJ, UK*

² *Department of Astronomy and Astrophysics, Pennsylvania State University, 525 Davey Lab, University Park, PA 16802, USA*

³ *Institute for Gravitation and the Cosmos, The Pennsylvania State University, University Park, PA 16802, USA*

Accepted ?; Received ??; in original form ???

ABSTRACT

Observations of the redshifted 21 cm line with upcoming radio telescopes promise to transform our understanding of the cosmic reionization. To unravel the underlying physical process, we investigate the 21 cm structures of three different ionizing sources, Population (Pop) III stars, the first galaxies, and the first quasars, by using radiative transfer simulations that include both ionization of neutral hydrogen and resonant scattering of Ly α photons. We find that Pop III stars and quasars produce a smooth transition from an ionized and hot state to a neutral and cold one, owing to their hard spectral energy distribution with abundant ionizing photons, in contrast to the sharp transition in galaxies. Furthermore, Ly α scattering plays a dominant role in producing the 21 cm signal as it determines the relation between hydrogen spin temperature and gas kinetic temperature. This effect, also called Wouthuysen-Field coupling, depends strongly on the ionizing source. It is the strongest around galaxies, where the spin temperature is highly coupled to that of the gas, resulting in extended absorption troughs in the 21 cm brightness temperature. On the other hand, in the case of Pop III stars, the 21 cm signal shows both emission and absorption regions around a small HII bubble. For quasars, a large emission region in the 21 cm signal is produced, and the absorption region decreases as the size of the HII bubble becomes large due to the limited traveling time of photons. We predict that future surveys from large radio arrays such as MWA, LOFAR and SKA may be able to detect the 21 cm signals of primordial galaxies and quasars, but not likely Pop III stars due to its small angular diameter.

Key words: radiative transfer – diffuse radiation – galaxies: evolution – galaxies: formation – galaxies: high-redshift – quasars: supermassive black holes

1 INTRODUCTION

The epoch of reionization (EoR), during which high energy photons produced by the first luminous objects reionized the neutral hydrogen in the intergalactic medium (IGM), was an important milestone in cosmic history (Loeb & Barkana 2001). The latest measurements from the Planck satellite suggest that the Universe was reionized at redshift $z \sim 11$ (Planck Collaboration 2013), in agreement with the seven-year results of Wilkinson Microwave Anisotropy Probe (WMAP) (Komatsu et al. 2011), while studies of Gunn-Peterson absorption (Gunn & Peterson 1965) of high-redshift quasars (QSOs) suggest that reionization began as

early as $z \sim 15$ and ended at $z \sim 6$ (Fan et al. 2006a). The reionization history strongly constrains not only the formation of the first generation of galaxies and QSOs, but also their feedback and impacts on structure formation at later times (Bromm & Yoshida 2011).

Over the past few years, impressive progress has been made in detecting distant objects. Recent observations using both broad-band colors (e.g., Bouwens et al. 2012; Ellis et al. 2013) and narrow-band Ly α emission (e.g., Ouchi et al. 2010; Kashikawa et al. 2011) have detected hundreds of galaxies at $z \gtrsim 6$. Meanwhile, over two dozen luminous QSOs have been detected at $z \sim 6$ (e.g., Fan et al. 2006b; Willott et al. 2010b; Mortlock et al. 2011). While it is generally believed that early star-forming galaxies played an important role in reionizing the Universe (Robertson et al. 2010), the ionization process and the

* E-mail: yajima@roe.ac.uk (HY)

† Scottish Universities Physics Alliance

actual contributions from different ionizing sources remain poorly understood.

The 21 cm hyperfine line of neutral hydrogen has been proposed as a powerful tool to probe the EoR, as it traces the thermal history of the IGM and the ionization structures (e.g., Morales & Wyithe 2010; Pritchard & Loeb 2012). Recent advances in radio instrumentation and techniques will soon make it possible to measure the highly redshifted 21 cm line from gas during the first billion years after the Big Bang, as a number of radio interferometers are currently being built or planned, such as Murchison Widefield Array (MWA; Lonsdale et al. 2009), the LOw Frequency ARray (LOFAR; Harker et al. 2010), the Precision Array to Probe the Epoch of Reionization (PAPER; Parsons et al. 2010), the Giant Meter-wave Radio Telescope (GMRT; Paciga et al. 2011), and the Square Kilometre Array (SKA; Dewdney et al. 2009).

In order to understand and interpret observations from these instruments, it is critical to understand the 21 cm structures from different ionizing sources. It has been suggested by advanced numerical simulations that the first stars (so-called ‘‘Population III’’ stars) started to form in mini-halos of $10^{5-6} M_{\odot}$ as early as $z \sim 30$ (Abel et al. 2002; Bromm et al. 2002; Yoshida et al. 2008; Turk et al. 2009; Clark et al. 2011). The first galaxies are believed to have formed in low-metallicity halos via gas accretion or mergers around $z \sim 15$ thanks to feedback and metal enrichment from Population (Pop) III stars (Wise & Abel 2007; Wise et al. 2008; Wise & Abel 2008; Greif et al. 2010; Pawlik et al. 2011; Wise et al. 2012). Meanwhile, the massive black holes (BHs) may have formed from remnants of massive Pop III stars or direct collapse of gas clumps or supermassive stars (e.g., Volonteri & Begelman 2010, leading to the emergence of the first QSOs (Li et al. 2007; Di Matteo et al. 2008; Sijacki et al. 2009; Di Matteo et al. 2012). These objects provided strong UV radiation that reionized the neutral hydrogen.

To date, a number of theoretical works have studied the 21 cm signals of Pop III stars (Chen & Miralda-Escudé 2004, 2008; Tokutani et al. 2009), galaxies (Furlanetto & Oh 2006; McQuinn et al. 2006; Kuhlen et al. 2006; Mellema et al. 2006; Semelin et al. 2007; Baek et al. 2010; Vonlanthen et al. 2011; Mesinger et al. 2011; Iliev et al. 2012), and QSOs (Wyithe et al. 2005; Wyithe & Loeb 2007; Geil & Wyithe 2008; Alvarez et al. 2010; Datta et al. 2012; Majumdar et al. 2012). The 21 cm signal can be emission or absorption against the cosmic microwave background (CMB), if spin temperature (T_{S}) is above or below the CMB temperature (T_{CMB}). The scattering process of Ly α photons is the main mechanism which causes T_{S} decouple from T_{CMB} via the Wouthuysen-Field effect (Wouthuysen 1952; Field 1958; Hirata 2006). Therefore, it is crucial to take into account Ly α scattering in the calculation of 21 cm signals. The Ly α radiation field in a moving medium like the Hubble flow is difficult to estimate analytically, because the diffuse approximation is no longer valid in a partially ionized or moving medium with higher relative velocity (Loeb & Rybicki 1999), and so must be determined through detailed radiative transfer (RT) calculations. However, despite the importance of the Wouthuysen-Field effect, the Ly α radiation field was simply modeled or completely ignored in most of the previous work; only a few actually

included Ly α RT in the estimate of T_{S} (e.g., Baek et al. 2010; Vonlanthen et al. 2011). In particular, Baek et al. (2009) and Baek et al. (2010) combined cosmological simulations and post-processing Ly α RT to calculate the 21 cm signals from UV and X-ray sources. They found that the absorption phase of the 21 cm survives throughout the EoR even in the presence of strong X-ray sources, and that the brightness temperature fluctuation of the 21 cm signal evolves strongly with redshift, with a higher amplitude in the early reionization phase.

In order to investigate the Wouthuysen-Field effect from different ionizing sources and the resulting 21 cm structures, we carry out here a comparative study of the ionization history of three types of sources: Pop III stars, primordial galaxies and QSOs. We perform RT calculations, which include both ionization and Ly α scattering, on individual sources embedded in the IGM. Different intrinsic spectral energy distributions (SEDs) appropriate for each source type are used. We follow the evolution of the ionization structures and temperature to derive the 21 cm signals.

The paper is organized as follows. In §2, we describe the model and methodology underlying our simulations. In §3, we present the results, which include the structure of ionization, temperatures and the 21 cm signal around different sources, and their time evolution. We discuss in §4 the detectability of the 21 cm structures of these sources by upcoming facilities such as MWA, LOFAR and SKA, and we summarize in §5.

2 MODEL & METHOD

In this work, we carry out RT calculations that include ionization and Ly α scattering on three types of ionizing sources embedded in the IGM: Pop III stars, galaxies, and QSOs. The IGM is modeled as spherical shells around the source. The boundary of the sphere is set to $R = 7R_{\text{S}}$, where R_{S} is the radius of Strömrgren sphere, and it is linearly divided into 300 bins.

For each source type, we consider a range of masses in the redshift range $z = 7 - 20$. For Pop III stars, $M_{\text{star}} = 2 \times 10^2 - 2 \times 10^5 M_{\odot}$; for galaxies, $M_{\text{star}} = 2 \times 10^6 - 2 \times 10^{10} M_{\odot}$, and for QSOs, $M_{\text{star}} = 2 \times 10^8 - 2 \times 10^{12} M_{\odot}$, where M_{star} is total stellar mass. For Pop III stars with $M_{\text{star}} > 10^2 M_{\odot}$, we assume multiple star formation of $100 M_{\odot}$ in a halo (e.g., Greif et al. 2012), or a cluster of halos with Pop III stars.

2.1 The 21 cm Signal

The fluctuation in 21 cm intensity (or fluctuation of brightness temperature) from different regions of the IGM at a given redshift z depends sensitively on the gas properties, including density, velocity gradients, gas temperature, gas spin temperature and ionization state (Furlanetto & Oh 2006). We follow the procedure of previous works (e.g., Furlanetto & Oh 2006; Baek et al. 2009) which calculate the fluctuation of the brightness temperature as

$$\delta T_{\text{b}} = 28.1 \chi_{\text{HI}} (1 + \delta) \left(\frac{1+z}{10} \right)^{1/2} \frac{T_{\text{S}} - T_{\text{CMB}}}{T_{\text{S}}} \text{ mK}, \quad (1)$$

where χ_{HI} is the neutral hydrogen fraction, δ is over density, T_{S} and T_{CMB} are the gas spin and CMB temperature respectively. The IGM is assumed to be uniform, i.e., $\delta = 0$, as recent simulations suggest small clumpiness in the IGM at high redshift (Pawlik et al. 2009). The contribution of the gradient of the proper velocity is not considered in this work.

The gas spin temperature is controlled by Thomson scattering of CMB photons, Ly α photon pumping, and collisions by the gas particles, as formulated by Furlanetto & Oh (2006):

$$T_{\text{S}}^{-1} = \frac{T_{\text{CMB}}^{-1} + x_{\text{C}}T_{\text{gas}}^{-1} + x_{\alpha}T_{\text{C}}^{-1}}{1 + x_{\text{C}} + x_{\alpha}}, \quad (2)$$

where T_{C} is the color temperature of the Ly α line, T_{gas} is the kinetic temperature of the gas, x_{α} and x_{C} are the coupling coefficients by Ly α photon scattering and gas collision respectively, which are calculated for each spherical shell from RT simulations of ionizing and Ly α photons as follows

$$x_{\alpha} = \frac{4P_{\alpha}T_{\star}}{27A_{10}T_{\text{CMB}}}, \quad (3)$$

$$x_{\text{C}} = \frac{T_{\star}}{A_{10}T_{\text{CMB}}}(C_{\text{H}} + C_{\text{p}} + C_{\text{e}}). \quad (4)$$

where $T_{\star} = 0.068$ K, $A_{10} = 2.85 \times 10^{-15} \text{ s}^{-1}$ is the spontaneous emission factor of the 21 cm transition, P_{α} is the number of scatterings of Ly α photons per atom per second, and C_{H} , C_{p} and C_{e} are the de-excitation rates due to collision with neutral atoms, protons, and electrons, respectively. We use the fitting formula given by Liszt (2001) and Kuhlen et al. (2006) for the de-excitation rates.

Since T_{C} quickly settles into T_{gas} owing to the recoil effect of Ly α photon scattering, $T_{\text{C}} = T_{\text{gas}}$ is assumed in our calculations. The spin temperature depends sensitively on the coupling due to Ly α scattering and collision. When the coupling is strong, it decouples from the CMB temperature and becomes $T_{\text{S}} \sim T_{\text{gas}}$.

2.2 Intrinsic SEDs of Ionizing Sources

We consider different SEDs for the three types of sources, PopIII stars, galaxies, and QSOs in our calculations. For PopIII stars, we assume a black body spectrum, and follow the formulae from Bromm et al. (2001a) to calculate the effective temperature and bolometric luminosity of a star with mass M :

$$T_{\text{PopIII}}^{\text{eff}} = 1.1 \times 10^5 \left(\frac{M}{100 M_{\odot}} \right)^{0.025} \text{ K}, \quad (5)$$

$$L_{\text{PopIII}}^{\text{bol}} = 10^{4.5} \frac{M}{M_{\odot}} L_{\odot}. \quad (6)$$

Halo hosting Pop III stars can be metal-enriched quickly due to type-II or pair-instability supernovae (Wise et al. 2012; Johnson et al. 2013). As a result, metallicity can exceed the threshold of Pop III star formation, $Z/Z_{\odot} \sim 10^{-3.5}$ (Bromm et al. 2001b), and then Pop II stars form in halos (e.g., Wise et al. 2012). On the other hand, recent simulations showed that multiple Pop III stars form in each halo (Clark et al. 2011; Greif et al. 2012), and haloes are clustered close together (Umemura et al. 2012). In addition, if the mass of Pop III stars is $\gtrsim 260 M_{\odot}$, they collapse directly into black holes (Heger & Woosley 2002), as a result, the halo can keep making Pop III stars even after several

Myr. Hence, in this work, we assume Pop III halos which consist of Pop III stars alone. Effects of mixed systems of Pop III and Pop II stars on 21 cm signal will be investigated by detailed hydrodynamics simulations in future work.

The primordial galaxies in our model are assumed to consist of only young, metal-poor stars which follow a Salpeter initial mass function (IMF) (Salpeter 1955). We assume a stellar age of 10 Myr and a metallicity of $Z = 0.1 Z_{\odot}$, which are consistent with observations of high-redshift Ly α emitting galaxies (e.g., Lai et al. 2007; Finkelstein et al. 2009; Ota et al. 2010; Nakajima et al. 2012). The SEDs of galaxies are then generated using the stellar population synthesis code PÉGASE v2.0 (Fioc & Rocca 1997) for a given stellar mass with the above parameters of stellar age, metallicity and IMF. In practice, the SED changes with evolution time. However, the star formation history of high-redshift galaxies is as yet poorly understood. In this work, for simplicity, we use the above SED with constant age, metallicity and stellar mass. Note that, however, even if we consider an evolving SED with a constant star formation model like SFR = $(M_{\text{star}}/10^8 M_{\odot}) M_{\odot} \text{ yr}^{-1}$ (e.g., Ono et al. 2010), the differences of sizes of HII bubbles are within a factor of ~ 2 .

The SED of QSOs is estimated by adding a broken power-law spectrum of massive black holes to the galaxy's SED. The power-law spectrum is assumed, following Laor & Draine (1993); Marconi et al. (2004); Hopkins et al. (2007), to be

$$\nu L_{\nu} \propto \begin{cases} \nu^{1.2} & \text{for } \log(\nu/\text{Hz}) < 15.2 \\ \nu^{-1.2} & \text{for } \log(\nu/\text{Hz}) > 15.2. \end{cases} \quad (7)$$

Recent observations of the most distant QSOs show that the BH accretion rates are close to the Eddington limit (Willott et al. 2010a), and simulations of early QSOs by Li et al. (2007) showed that the mass ratio of BHs to stars in the hosts is $\sim 10^{-3}$, similar to that of local galaxies (e.g., Marconi & Hunt 2003; Rix et al. 2004). Therefore, in our QSO model, the BH mass is set to be $M_{\text{BH}} \sim 10^{-3} \times M_{\text{star}}$, and its luminosity is derived assuming an Eddington limit. For ionization and heating, we integrate the above SED up to 40 KeV. Contribution of higher-energy photons $E > 40$ KeV is negligible because of the small energy fraction and low ionization cross section. In addition, free electrons made by X-ray ionization are highly energetic, and they make Ly α photons via collisions with neutral hydrogen. Roughly 40 per cent of X-ray energy can be used for the production of Ly α photons, and they can enhance the 21 cm signal (Chen & Miralda-Escudé 2008). We also include the additional Ly α photons by converting 40 per cent of X-ray energy at $E > 0.1$ KeV.

The SEDs of these three types of sources are shown in Figure 1. Pop III stars have a hard SED with a peak at $\lambda \sim 300 \text{ \AA}$. The SED of galaxies drops sharply at wavelengths shortward of the Lyman limit $\lambda \sim 912 \text{ \AA}$, while that of QSO has a power-law tail from X-rays to the Lyman limit owing to radiation from an accreting BH. As we will show later, the difference in the SEDs at $\lambda \lesssim 912 \text{ \AA}$ would result in different ionization structures of hydrogen by the three ionizing sources. On the other hand, both galaxies and QSOs have much higher continuum flux between Ly α and Ly β frequencies than Pop III stars, which would lead to stronger effects of Ly α scattering.

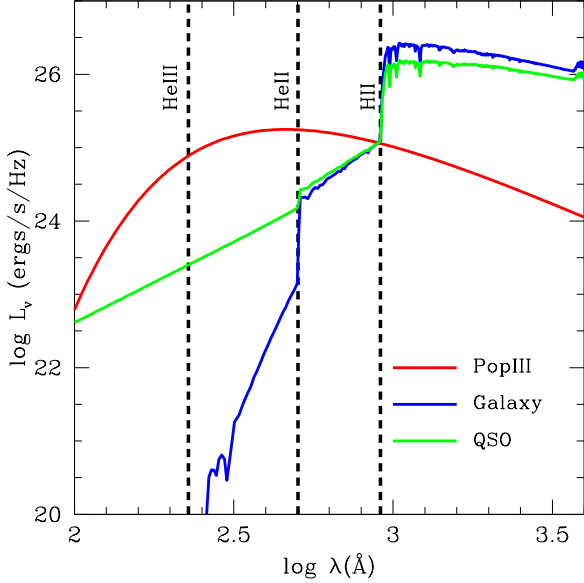


Figure 1. The intrinsic SEDs of a Pop III star (red curve), a galaxy (blue curve), and a QSO (green curve). The SEDs of the Pop III star and QSO are normalized by the flux of galaxy with $M_{\text{star}} = 10^6 M_{\odot}$ at 900 \AA . The three vertical dashed lines indicate the wavelengths of HeII, HeI and HII, respectively.

2.3 Ionization and Heating of the IGM

We calculate the ionization of hydrogen and helium in the IGM by central sources using one-dimensional RT of ionizing photons. Recent simulations showed that the escape fraction of ionizing photons (f_{esc}) of high-redshift galaxies or Pop III halos can be $\gtrsim 0.5$ (Yoshida et al. 2007; Wise & Cen 2008; Yajima et al. 2011; Paardekooper et al. 2013). Hence, we simply assume that half of ionizing photons are absorbed by the interstellar medium (ISM) and the rest escape from halos and ionize IGM. About 0.68 of ionizing photons absorbed by ISM or IGM are converted to Ly α photons via recombination processes. Here we ignore detailed ionization structure in halos of which the spatial scale is much smaller than the typical size of HII bubbles in the IGM. In addition, we focus on the early phase when the radiation field is localized, hence the radiation background from external sources is not included. The time evolution of the ionization of hydrogen and helium is estimated by the following equations:

$$\frac{d\chi_{\text{HI}}}{dt} = -\Gamma_{\text{HI}}^{\gamma} - \Gamma_{\text{HI}}^{\text{C}}\chi_{\text{HI}}n_e + \alpha_{\text{B}}^{\text{H}}\chi_{\text{HI}}n_e, \quad (8)$$

$$\frac{d\chi_{\text{HeI}}}{dt} = -\Gamma_{\text{HeI}}^{\gamma} - \Gamma_{\text{HeI}}^{\text{C}}\chi_{\text{HeI}}n_e + \alpha_{\text{B}}^{\text{HeI}}\chi_{\text{HeI}}n_e, \quad (9)$$

$$\begin{aligned} \frac{d\chi_{\text{HeII}}}{dt} &= \Gamma_{\text{HeI}}^{\gamma} - \Gamma_{\text{HeII}}^{\gamma} + \Gamma_{\text{HeI}}^{\text{C}}\chi_{\text{HeI}}n_e - \Gamma_{\text{HeII}}^{\text{C}}\chi_{\text{HeII}}n_e \\ &\quad - \alpha_{\text{B}}^{\text{HeI}}\chi_{\text{HeII}}n_e + \alpha_{\text{B}}^{\text{HeII}}\chi_{\text{HeII}}n_e. \end{aligned} \quad (10)$$

Here, χ_{HI} , χ_{HeI} , χ_{HII} , and χ_{HeII} are the ionization fractions of neutral hydrogen, neutral helium, ionized hydrogen and ionized helium, respectively, n_e is the electron density, α_{B} is the case B recombination rate, Γ^{C} is the collisional ionization rate. We use the fitting formula of Gnedin & Ostriker

(1997) for α_{B} , and that of Cen (1992) for Γ^{C} . The photo-ionization rate Γ^{γ} in each shell is estimated by

$$\Gamma_{\text{HI}}^{\gamma} = \frac{1}{n_{\text{H}}V_{\text{shell}}} \int_{\nu_{\text{limit}}}^{\infty} \frac{L(\nu)}{h\nu} e^{-\tau(\nu)} (1 - e^{-\Delta\tau_{\text{HI}}(\nu)}) d\nu \quad (11)$$

where V_{shell} is the volume of the gas shell, ν_{limit} is the Lyman limit frequency, τ is the optical depth from the central source to the shell, and $\Delta\tau$ is optical depth of the shell. The optical depth is calculated by

$$\begin{aligned} \tau(\nu) &= n_{\text{H}}\sigma_{\text{HI}}(\nu) \int_0^r dr' \chi_{\text{HI}}(r') + n_{\text{He}}\sigma_{\text{HeI}}(\nu) \int_0^r dr' \chi_{\text{HeI}}(r') \\ &\quad + n_{\text{He}}\sigma_{\text{HeII}}(\nu) \int_0^r dr' \chi_{\text{HeII}}(r') \end{aligned} \quad (12)$$

where σ is the ionization cross section. We use the fitting formula from Cen (1992), $\sigma_{\text{HI}} = 6.3 \times 10^{-18} (\nu/\nu_{\text{limit}}^{\text{HI}})^{-3}$, $\sigma_{\text{HeI}} = 7.2 \times 10^{-18} [1.66(\nu/\nu_{\text{limit}}^{\text{HeI}})^{-2.05} + 0.66(\nu/\nu_{\text{limit}}^{\text{HeI}})^{-3.05}]$, $\sigma_{\text{HeII}} = 1.58 \times 10^{-18} (\nu/\nu_{\text{limit}}^{\text{HeII}})^{-3}$.

The evolution of ionization would lead to change of gas temperature in each shell with time as follows,

$$\frac{dT_{\text{gas}}}{dt} = \frac{2}{3k_{\text{B}}n} \left[k_{\text{B}}T_{\text{gas}} \frac{dn}{dt} + H - \Lambda \right] \quad (13)$$

where k_{B} is the Boltzmann constant, n is the total number density of hydrogen and helium, H is the heating rate, and Λ is the cooling rate. We follow the procedures of Maselli et al. (2003) to calculate the heating and cooling rates: we consider photo-heating for H , while for Λ , we include recombination, collisional ionization and excitation cooling processes. The upper limit of the gas temperature is set to 10^5 K, and heating by Ly α photon scattering is not included, as it was shown to be insignificant by Chen & Miralda-Escudé (2004).

We follow the evolution of ionization and temperature up to 10^8 yr, and we calculate the Ly α radiation field and the 21 cm signal of the snapshots at $t_{\text{evo}} = 10^6, 10^7$ and 10^8 yr. Our fiducial runs use the snapshot at $t_{\text{evo}} = 10^7$ yr at redshift $z = 10$.

2.4 Radiative Transfer of Ly α Photons

The RT of Ly α photons in IGM is a highly complex process. It depends strongly on the Ly α resonant scattering, and on the density distribution and ionization state of the medium. The frequency change resulting from the scattering is difficult to estimate analytically. Yajima et al. (2012a) has developed a three-dimensional, Monte Carlo Ly α RT code which couples the continuum and ionization of hydrogen. Here we use the 1-D version of the code to numerically simulate the Ly α RT in spherical shells of the IGM.

In the scattering process, the outgoing frequency in the laboratory frame ν^{out} is calculated as

$$\frac{\nu^{\text{out}} - \nu_0}{\Delta\nu_{\text{D}}} = \frac{\nu^{\text{in}} - \nu_0}{\Delta\nu_{\text{D}}} - \frac{v_a \cdot k_{\text{in}}}{v_{\text{th}}} + \frac{v_a \cdot k_{\text{out}}}{v_{\text{th}}} \quad (14)$$

where ν^{in} is the incoming frequency in the rest frame of scattering medium, ν_0 is the line center frequency $\nu_0 = 2.466 \times 10^{15}$ Hz, v_a is the atom velocity, $\Delta\nu_{\text{D}} = (v_{\text{th}}/c)\nu_0$ corresponds to the Doppler frequency width, v_{th} is the velocity dispersion of the Maxwellian distribution describing the thermal motions, i.e., $v_{\text{th}} = (2k_{\text{B}}T/m_{\text{H}})^{1/2}$, and k_{in} and k_{out} are the incoming and outgoing propagation directions, respectively.

We consider Ly α photons from both continuum radiation of sources and recombination processes in ionized ISM and IGM. The intrinsic Ly α luminosity is estimated by

$$L_{\text{Ly}\alpha} = \int_{912 \text{ \AA}}^{1216 \text{ \AA}} P_{\text{abs}} f_{\text{conv}} L_{\lambda} d\lambda + 0.68 h\nu_{\alpha} (1 - f_{\text{esc}}) \dot{N}_{\text{Ion}} + 0.68 h\nu_{\alpha} \alpha_{\text{B}}^{\text{H}} n_{\text{HII}} n_{\text{e}} V_{\text{I}} \quad (15)$$

where the continuum spectrum is considered in the frequency range from the Ly α line (1216 Å) to Lyman limit (912 Å), P_{abs} is the absorption fraction in the calculation boxes, f_{conv} is the conversion fraction to Ly α photons via the cascade decay from higher quantum levels to the ground state (Hirata 2006), and ν_{α} is the Ly α frequency. The Ly α from ISM is simply proportional to number of absorbed ionizing photons because of short recombination time-scale in ISM, while that from IGM depends on the volume of the ionized bubble V_{I} and the density of the ionized hydrogen and electrons. Photons in this continuum range can be absorbed by neutral hydrogen which is then excited to higher levels of the Lyman series, and some of hydrogen atoms can transit from the 2p to the 1s state by emitting Ly α photons. Since we focus on the early phase of ionization up to 10^8 yr in this work, which is shorter than the recombination time scale in IGM ($t_{\text{rec}} \sim 4 \times 10^8$ yr), the ionized volume V_{I} in Equation 15 is generally smaller than the Strömgren sphere at ionization equilibrium. Hence, the Ly α emission from IGM is much smaller than the other components. The Ly α emission from ISM is dominant for Pop III stars due to the high effective temperature, while the contribution of the continuum radiation is dominant for galaxies and QSOs.

We simulate the Ly α RT using the structure of ionization and temperature at times $t_{\text{evo}} = 10^6, 10^7$ and 10^8 yr, by assuming that the travel time of the Ly α photons $t_{\text{travel}} = t_{\text{evo}}$. We divide the Ly α radiative transfer calculations into two parts. First, we calculate the RT of Ly α photons from the recombination process which are emitted from central sources. These Ly α photons diffusely propagate outward. We performed a convergence test and found an optimal number of photon packets for the RT calculations, $N_{\text{p}} = 10^5$, of which the number of Ly α photons $N_{\text{Ly}\alpha} = L_{\text{Ly}\alpha} / (h\nu_{\alpha} N_{\text{p}})$. In these calculations, since we need to estimate the rate of scattering of Ly α photons in each shell precisely to derive the spin temperature, we can not use the ‘‘core skipping’’ technique in the Ly α RT which can accelerate the calculation, as used in most Ly α RT simulations (e.g., Zheng & Miralda-Escudé 2002; Verhamme et al. 2006; Dijkstra et al. 2006; Laursen et al. 2009; Yajima et al. 2012b, 2013). Hence, the calculations are very expensive even with 10^5 photon packets. Each simulation took a few days running on 64 processors. Second, we consider continuum photons between Ly α and Lyman limit frequencies. Total energy of these photons is larger than that of the recombination photons in the cases of galaxies and QSOs. Unlike the Ly α photons from the recombination process, the continuum photons can travel for long distances until they are absorbed at the Lyman series frequencies after cosmological redshifting (Pritchard & Furlanetto 2006; Vonlanthen et al. 2011). For example, at $z \sim 10$, the photons for which the frequency is just below Ly β can travel ~ 40 Mpc before the frequency is shifted to Ly α . Once they

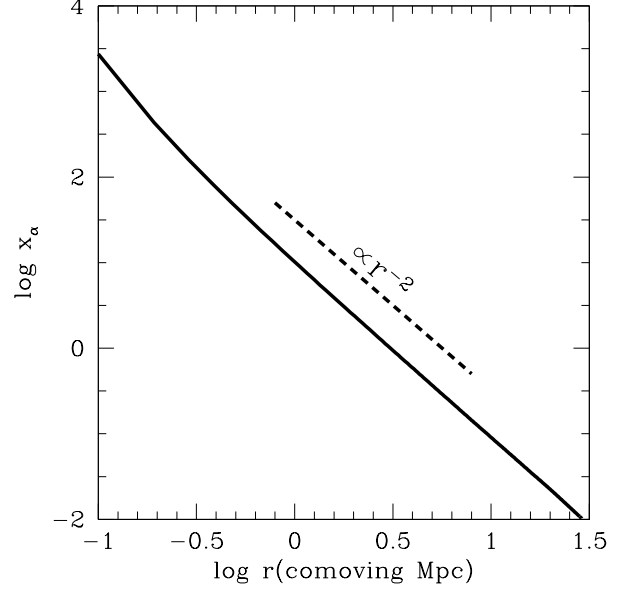


Figure 2. Profile of the coupling coefficient by continuum photons as a function of radial distance from a QSO of $M_{\text{star}} = 2 \times 10^8 M_{\odot}$ at $z = 10$. Uniform IGM density on Hubble flow is assumed.

are trapped, some fraction are converted to Ly α photons after the cascade decay (Hirata 2006) and experience numerous scatterings. Baek et al. (2009) showed the number of scattering at the trapped place could be approximated by $N_{\text{sca}} = 8 \times 10^5 H(z=10)/H(z)$, ignoring spatial diffusion. We use this approximation for the continuum photons. For uniform density and temperature, the scattering rate per atom by the continuum photons decreases with the r^{-2} profile as the radial distance from sources becomes large (Pritchard & Furlanetto 2006; Chuzhoy & Zheng 2008; Semelin et al. 2007; Naoz & Barkana 2008). As shown in Figure 2, we also test the distribution of the coupling coefficient by continuum photons and show the roughly r^{-2} distribution for a case of QSO of $M_{\text{star}} = 2 \times 10^8 M_{\odot}$ in uniform IGM on Hubble flow at $z = 10$, which is similar to the test calculation of Semelin et al. (2007) (other test calculations were shown in Yajima et al. 2012a). The slight difference from the r^{-2} profile is due to the not flat SEDs shown in Figure 1.

3 RESULTS

We performed a set of RT simulations on three types of ionizing sources, Pop III star, primordial galaxy and QSO, in the redshift range $z = 7-20$. A wide range of masses were considered for these sources: $M_{\text{star}} = 2 \times 10^2 - 2 \times 10^5 M_{\odot}$ for Pop III stars or cluster of Pop III stars, $M_{\text{star}} = 2 \times 10^6 - 2 \times 10^{10} M_{\odot}$ for galaxies, and $M_{\text{star}} = 2 \times 10^8 - 2 \times 10^{12} M_{\odot}$ for QSOs.

3.1 Structures of Ionization and Temperature

The propagation of the ionization front of a Pop III star, a primordial galaxy, and a QSO are shown in Figure 3, in

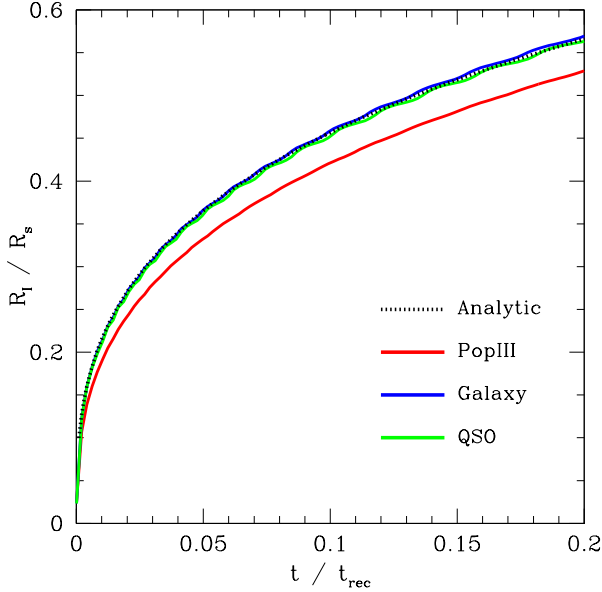


Figure 3. Propagation of the ionization front (normalized by radius of the Strömgren sphere) as a function of time (normalized by recombination timescale), for a Pop III star ($M_{\text{star}} = 2 \times 10^2 M_{\odot}$, red), a galaxy ($M_{\text{star}} = 2 \times 10^6 M_{\odot}$, blue), and a QSO ($M_{\text{star}} = 2 \times 10^8 M_{\odot}$, green), respectively. The black dotted line is the analytical solution from Spitzer (1978).

comparison with the analytical solution from Spitzer (1978). The position of the ionization front is measured where the ionized hydrogen fraction $\chi_{\text{HII}} = 0.5$. The size of the ionized region from the galaxy and QSO follows the analytical one closely, but that of the Pop III star appears to be smaller, owing to helium ionization by Pop III stars. As shown in Figure 1, the SED of Pop III stars peaks around the Lyman limit frequency of HeII, hence a fraction of the ionizing photons is consumed by helium ionization, resulting in a smaller HII region compared to the analytical solution which assumes that all the ionizing photons are absorbed by neutral hydrogen.

The resulting structures of the ionization, temperatures and differential brightness temperature of the above ionizing sources are shown in Figure 4. The ionization structures of both the Pop III star and QSO show smooth transitions from ionized to neutral state for hydrogen, while the galaxy shows a sharp transition. This is because the high-energy photons of PopIII stars and QSOs have long mean free paths, and they can partially ionize the gas, making the transition smooth. Moreover, the hard SEDs of Pop III stars and QSOs can also produce ionized HeII regions, which is absent in the modeled galaxy without accreting black holes. The size of the ionized HeIII region is a fraction of ~ 0.2 of the HII bubble in Pop III stars and ~ 0.1 in QSOs.

Similarly, the temperatures show different structures from these different sources. The kinetic temperature of the gas, T_{gas} , shows a smooth transition from a hot ($\sim 10^4$ K) to cold (\sim a few K) state around the Pop III star and the QSO, in contrast to the sharp transition in the galaxy, due to partial ionization and heating from photoionization. The spin temperature T_{S} shows different patterns in these sources.

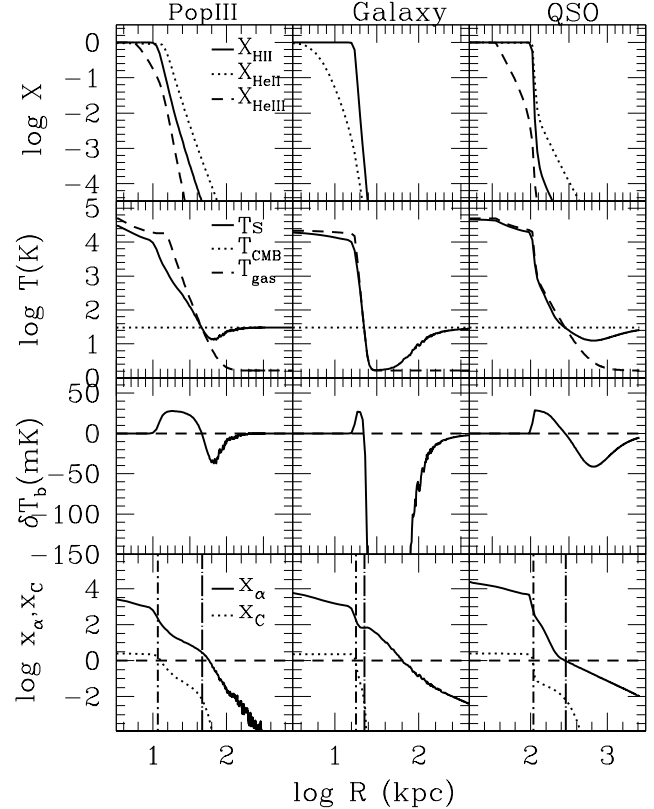


Figure 4. Structure of ionization, temperature, coupling coefficients by $\text{Ly}\alpha$ photons, and differential brightness temperature as a function of distance from the central source at redshift $z = 10$ for a Pop III star ($M_{\text{star}} = 2 \times 10^2 M_{\odot}$, left column), a galaxy ($M_{\text{star}} = 2 \times 10^6 M_{\odot}$, middle column), and a QSO ($M_{\text{star}} = 2 \times 10^8 M_{\odot}$, right column), respectively. The top row panels show the fraction of HII, HeII, and HeIII at $t_{\text{evo}} = 10^7$ yr, respectively. The second row panels show the temperatures of spin, gas and CMB, respectively. The third row panels are the fluctuations of brightness temperature. The bottom row panels represent the coupling coefficients x_{α} (by $\text{Ly}\alpha$ photon scattering, solid line) and x_{C} (by gas collision, dotted line). The dashed line represents unity. When the coupling coefficients are higher than unity, the spin temperature can decouple from the CMB temperature. The vertical dash-dot line indicates the location of the ionization front at $\chi_{\text{HII}} = 0.5$, while the long-dash-dot line indicates the location where $T_{\text{gas}} = T_{\text{CMB}}$. In region beyond the long-dash-dot line, if the coupling coefficient is higher than unity, then it would cause absorption, as is the case of the galaxy model.

As indicated in Equation 2, T_{S} depends strongly on the coupling efficiency due to $\text{Ly}\alpha$ scattering and gas collision. If the coupling is strong, T_{S} is coupled to T_{gas} which is in general different from the CMB temperature T_{CMB} . As shown in the second row panels of Figure 4, for the Pop III star, T_{S} is weakly coupled to T_{gas} within the HII region due to the small number of the $\text{Ly}\alpha$ scatterings resulted from low number of $\text{Ly}\alpha$ photons in its SED. As the $\text{Ly}\alpha$ scattering becomes sparse beyond the HII region, T_{S} is decoupled from T_{gas} and it takes the value of T_{CMB} . For the galaxy, T_{S} is completely coupled to T_{gas} at $R \lesssim 40$ kpc due to strong $\text{Ly}\alpha$ scattering, it is thus completely decoupled from T_{CMB} . For the QSO, T_{S} is tightly coupled to T_{gas} within $R \lesssim 300$ Kpc

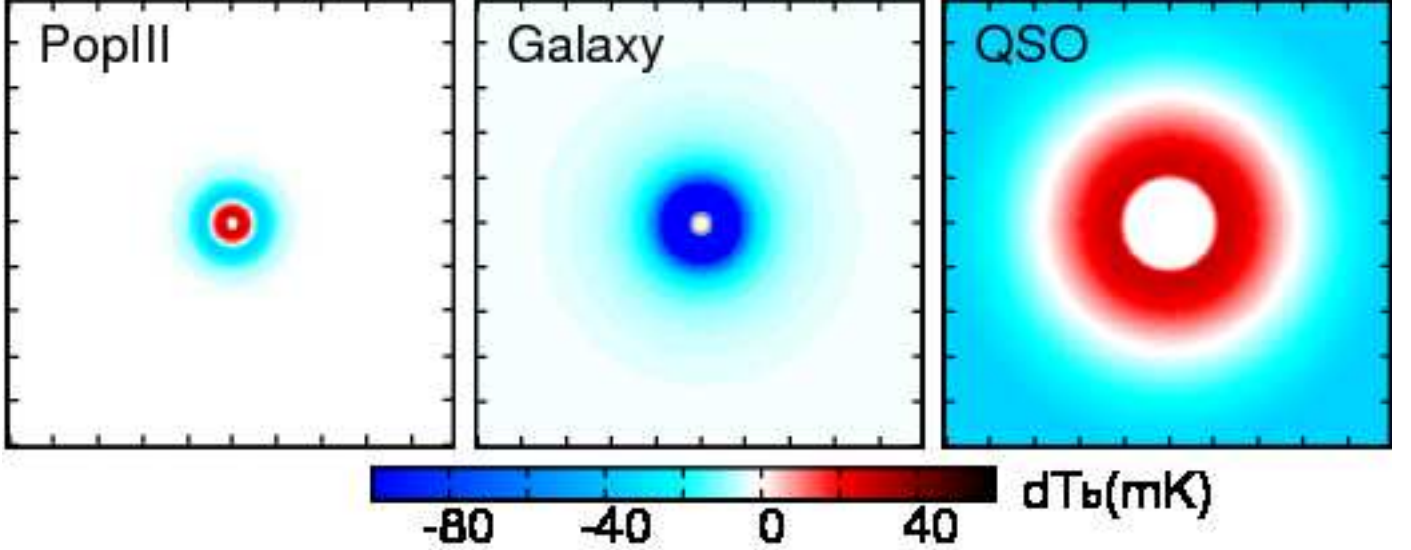


Figure 5. Two-dimensional map of the differential brightness temperature of Pop III stars ($M_{\text{star}} = 2 \times 10^2 M_{\odot}$), galaxy ($M_{\text{star}} = 2 \times 10^6 M_{\odot}$) and QSO ($M_{\text{star}} = 2 \times 10^8 M_{\odot}$) at $t_{\text{evo}} = 10^7$ yr. The box size is 500 kpc in physical scale.

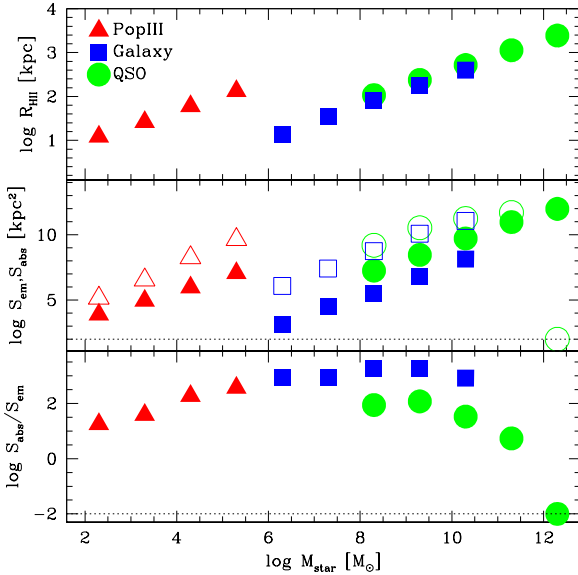


Figure 6. Dependence of the 21 cm structures on the source mass for Pop III stars (green triangles), galaxies (red squares), and QSOs (blue circles). *Upper panel*: size of the ionized bubble R_{HII} at $t_{\text{evo}} = 10^7$ yr, defined as the position at $\chi_{\text{HII}} = 0.5$. *Middle panel*: surface area of emission S_{em} (filled symbols) and absorption ring S_{abs} (open symbols). *Lower panel*: ratio of $S_{\text{abs}}/S_{\text{em}}$ as a function of stellar mass of the source. The dotted lines are artificial lower limits.

(\sim three times of the size of HII bubble), but outside of which it decouples from T_{gas} and becomes T_{CMB} due to the sharp decline of Ly α scattering.

As a result of the different ionization and temperature structures around the three sources, the 21 cm signal shows different features, as shown in δT_{b} in the lower panels in

Figure 4. The modeled galaxy shows a narrow emission ring surrounded by an extended absorption trough owing to efficient coupling between T_{S} and T_{gas} . In the case of Pop III star and QSO, since the travel of most Ly α photons from the recombination process is confined to the transition region with numerous resonant scatterings within the limited $t_{\text{evo}} = 10^7$ yr, the T_{gas} at transition region is higher than T_{CMB} , so they both show extended emission in δT_{b} in the transition region, and the QSO shows the extended absorption region due to continuum flux. However, due to the dilution of flux, the absorption signal is weak ($\delta T_{\text{b}} \lesssim 50$ K).

The 21 cm structure of QSOs from our model differs from that of Alvarez et al. (2010), which showed extended deep absorption shell in the outer cold region under the assumption of $T_{\text{S}} = T_{\text{gas}}$. In addition, Datta et al. (2012) used the assumption of $\delta T_{\text{b}} = 4.6 \times 10^4 \text{ K cm}^3 n_{\text{HI}}(z, \text{comoving}) \sqrt{z+1}$, which leads to emission even in the region far from QSOs. In the case of Pop III stars, the absorption feature from our calculations is shallower than that of Chen & Miralda-Escudé (2008). This is caused by a smaller P_{α} due to the limited traveling time of Ly α photons.

To further illustrate the physical process behind the emission and absorption features of the 21 cm signal, we show the radial profiles of the coupling coefficients caused by Ly α scatterings, x_{α} , and by gas collisions, x_{C} , respectively. When the coupling coefficient is higher than unity, the spin temperature can decouple from the CMB temperature. As can be seen, x_{C} is around unity in high-temperature region, and becomes very small in region with neutral hydrogen gas. As a result, gas collision has little effect on the change of T_{S} , the δT_{b} , in neutral region. On the other hand, x_{α} shows a much higher value than unity even in the outer neutral region, and it decreases steeply with distance, because the scattering cross section decreases due to high relative velocity, and Ly α photons emitted near sources cannot propagate to outer region within the limited travel time. On the other

hand, the continuum photons can propagate long distance until they are trapped as Lyman series photons due to the Doppler shift. Consequently, due to the contribution of Ly α photons traveling near the sources, the distribution of x_α shows complicated structure, not the simple r^{-2} profile. In the case of Pop III stars, x_α is $\sim 1 - 100$ in the partially ionized and moderately high temperature region $T_{\text{gas}} > T_{\text{CMB}}$. Therefore, in such a region, T_S is much higher than T_{CMB} , resulting in emission in δT_b . However, at the location of $T_{\text{gas}} \sim T_{\text{CMB}}$, x_α becomes ~ 3 , and less than unity in the cold region, leading to the shallower absorption structure. The x_α of the QSO case shows a similar trend with that of the Pop III star. However, since the continuum flux is much higher than for Pop III stars, these photons propagate a long distance and make the extended absorption region. In addition, we can see the r^{-2} profile in the outer region with these continuum photons. In the case of the galaxy, x_α appears to be very large (~ 70) at the location of $T_{\text{gas}} = T_{\text{CMB}}$, and it drops to ~ 1 at $R \sim 60$ kpc, resulting in the extended absorption region over a few hundreds kpc.

3.2 The 21 cm Structures

The resulting 21 cm maps of the Pop III star, galaxy, and QSO at $z = 10$ are shown in Figure 5. Clearly, the 21 cm structures of these different sources are distinctively different. The δT_b of the PopIII star shows a ring structure with emission in the inner region and absorption in the outer region. The galaxy shows a very thin emission ring but a deep, extended absorption region, while the QSO shows an extended emission ring and an outer weak absorption region.

To further investigate the dependence of 21 cm structures on source properties, we show the emission and absorption structures of the three sources at different stellar masses in Figure 6, as represented by the radius of the ionized bubble R_{HII} , the surface area of emission (S_{em}) and absorption (S_{abs}), and their ratio.

First, the size of the ionized region increases with the mass of the source, as shown in Figure 6 (top panel). This can be understood since the total number of ionizing photons is simply proportional to the cube-root of the total stellar mass in our models, $R_{\text{HII}} \propto M_{\text{star}}^{1/3}$. R_{HII} is in the range of $\sim 24 - 260$ kpc for PopIII stars, $\sim 27 - 792$ kpc for galaxies, and $\sim 0.2 - 4.9$ Mpc for QSOs. The size of the region ionized by QSOs is consistent with that from Wyithe et al. (2005). Pop III stars have a higher ionizing power because their hard SEDs produce more ionizing photons and higher effective temperature $\sim 10^5$ K. Of course, the ionized region would appear as a “zero-signal hole” ($\delta T_b \sim 0$ mK) in the 21 cm structure as shown in Figure 5.

The middle panel of Figure 6 shows the surface areas of the emission (S_{em}) and absorption (S_{abs}) regions in a two dimensional slice containing the central sources. For all models, S_{em} monotonically increases with the stellar mass of the source; the S_{abs} , however, is clearly different depending on the source type and the size of ionized region. The S_{abs} of galaxies are much higher than the S_{em} , which produces the strong absorption trough as seen in Figure 5. In the case of QSOs, S_{abs} decreases with increasing stellar mass at $M_{\text{star}} \gtrsim 10^{10} M_\odot$, since even continuum photons cannot propagate to the outside cold, neutral gas region in the limited time. The ratio between S_{abs} and S_{em} is shown in the lower panel

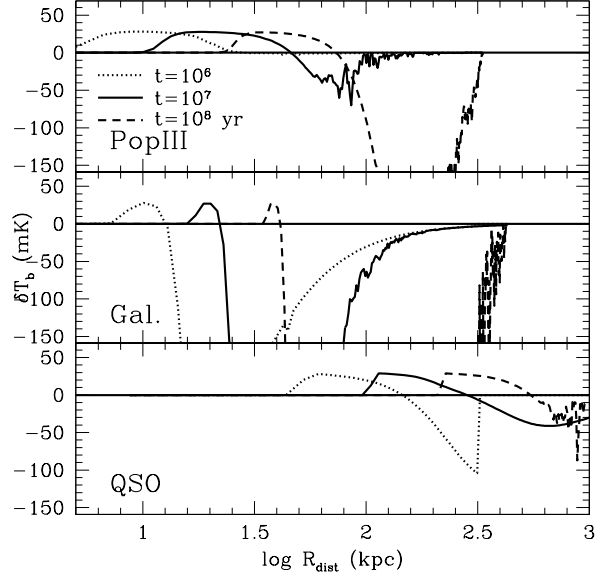


Figure 7. The evolution of the differential brightness temperature of a Pop III star, a galaxy, and a QSO at time $t_{\text{evo}} = 10^6, 10^7$ and 10^8 yr, respectively. The mass of these three sources is $M_{\text{star}} = 2 \times 10^2, 2 \times 10^6, 2 \times 10^8 M_\odot$, respectively.

of Figure 6. The ratio is in the range of $\sim 20 - 370$ for Pop III stars, $\sim 830 - 1850$ for the galaxies, and $\sim 0 - 120$ for the QSOs.

These results demonstrate that Pop III stars, the first galaxies, and the first QSOs have clearly different 21 cm structures, owing to different temperature and ionization structures resulting from different photon SEDs and propagation of Ly α photons in these regions.

3.3 Time Evolution of the 21 cm Structure

The evolution of the δT_b signal at different times is shown in Figure 7. As the ionizing bubble grows with time, the Ly α photons propagate into the more extended cold region through scattering, resulting in the stronger absorption signal. At $t_{\text{evo}} = 10^6$ yr, the δT_b of Pop III stars has no absorption region. At $t_{\text{evo}} = 10^8$ yr, all simulations show 21 cm absorptions. Note that for Pop III stars, the evolution of ionization may not last 10^8 yr due to their short lifetimes and fast metal enrichment (e.g., Wise et al. 2012). However, since the recombination time scale of IGM is longer than 10^8 yr, the Ly α photons can travel in the relic HII region and the cold region outside, which may produce similar absorption features as in Figure 7.

Figure 8 shows the evolution of the size of the ionizing bubble R_{HII} , surface area of emission S_{em} and absorption S_{abs} , and their ratio $S_{\text{abs}}/S_{\text{em}}$, at different time $t_{\text{evo}} = 10^6, 10^7$ and 10^8 yr for Pop III stars, galaxies, and QSOs. R_{HII} increases with t_{evo} , $R_{\text{HII}} \propto (1 - \exp(-t_{\text{evo}}/t_{\text{rec}}))^{1/3}$, where t_{rec} is recombination time scale. The S_{em} and S_{abs} of galaxies and QSOs show the slow increase with time, and the ratio of the two becomes nearly constant after $\sim 10^7$ years. In the case of Pop III stars, however, S_{abs} increases dramatically after $\sim 10^7$ years, leading to a strong absorption fea-

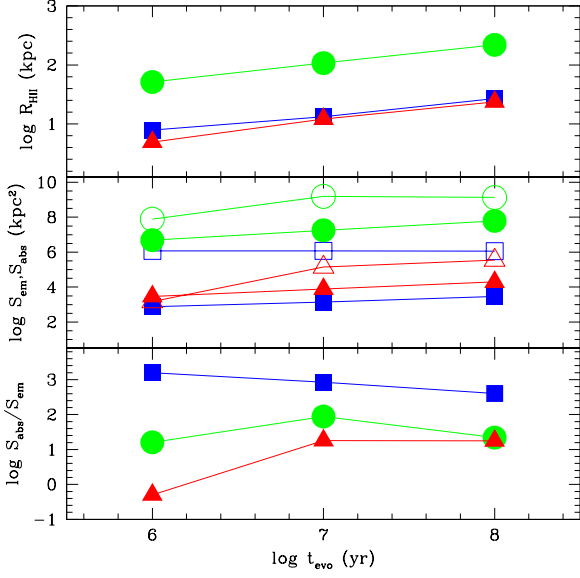


Figure 8. The evolution of the size of the ionizing bubble R_{HII} , surface area of emission S_{em} and absorption S_{abs} , and their ratio $S_{\text{abs}}/S_{\text{em}}$, at different times for Pop III stars (red triangles), galaxies (blue squares), and QSOs (green circles). The masses of these three different sources are $M_{\text{star}} = 2 \times 10^2, 2 \times 10^6, 2 \times 10^8 M_{\odot}$, respectively. The symbols are the same as in Figure 6.

ture. This is because $\text{Ly}\alpha$ photons from the recombination process are the dominant source of $\text{Ly}\alpha$ photon scatterings, and they are trapped near the source at $t \lesssim 10^7$ yr and can propagate to the outer cold region at $t \sim 10^8$ yr.

The probability distribution function (PDF) of the 21 cm emission volume is shown in Figure 9. As time evolves, more $\text{Ly}\alpha$ photons propagate to cold gas region, producing the extended tail of the PDF with the absorption signal. At $t_{\text{evo}} = 10^7$ yr, the PDF of Pop III stars is confined to $\delta T_{\text{b}} \gtrsim -80$ mK, and it extends to $\delta T_{\text{b}} < -100$ mK at 10^8 yr. In the case of the QSO, the PDF has the more extended tail at $\delta T_{\text{b}} \lesssim -160$ mK at $t_{\text{evo}} = 10^7$ yr due to the continuum photons.

3.4 Detectability

The detectability of the 21 cm emission from the first luminous objects with future instruments is of great interest. Here we calculate the detectability of the 21 cm emission from Pop III stars, first galaxies and quasars with upcoming observatories such as MWA, LOFAR, and SKA. The noise per resolution element is estimated by Furlanetto et al. (2009) as follows,

$$\Delta T \sim 20 \text{ mK} \left(\frac{10^4 \text{ m}^2}{A_{\text{eff}}} \right) \left(\frac{10'}{\Delta\theta} \right) \times \left(\frac{1+z}{10} \right)^{4.6} \left(\frac{\text{MHz}}{\Delta\nu} \frac{100 \text{ hr}}{t_{\text{int}}} \right)^{1/2}, \quad (16)$$

where A_{eff} is the effective collect area, $\Delta\theta$ is the angular diameter, $\Delta\nu$ is the band width, and t_{int} is the integration time.

For the redshifted 21-cm line at $z \sim 10$, the contribution from the polarized Galactic synchrotron foreground

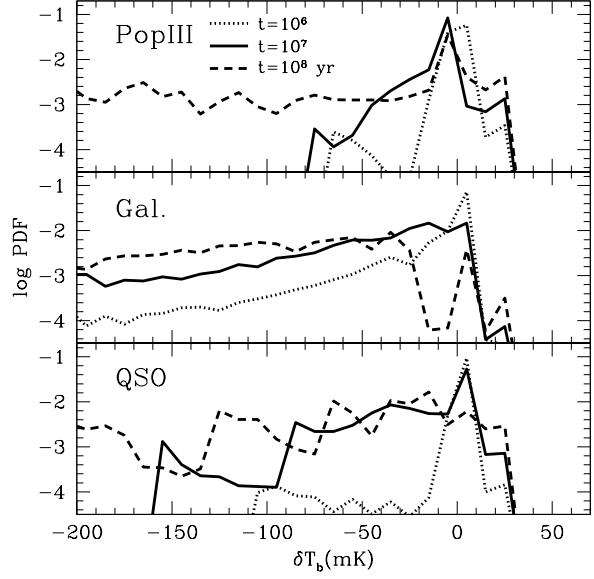


Figure 9. Probability distribution function (PDF) of the 21 cm emission volume normalized by the one of $5 \times$ Strömgren sphere. We derived the normalized emission volume of each stellar mass, and stacked the PDFs.

is dominant over the system temperature, and it has $T \sim 180(\nu/180 \text{ MHz})^{-2.6}$. The sensitivity curves are shown in Figure 10. The yellow shade with $A_{\text{eff}} = 10^4 \text{ m}^2$ roughly corresponds to the sensitivity of MWA and LOFAR, while that with $A_{\text{eff}} = 10^6 \text{ m}^2$ corresponds to the sensitivity of SKA.

Here, we measure the size of the emission or absorption spheres accompanying the modeled sources with boundaries of $|\Delta T_{\text{b}}| = 1$ mK. We calculate the δT_{b} map with thickness of $\Delta\nu = 1, 2, 3$ and 4 MHz around central sources, and we estimate $\langle \delta T \rangle$ by taking the absolute value of the spatial mean of δT_{b} at $t_{\text{evo}} = 10^7$ yr. The $\langle \delta T \rangle$ is not sensitive to the different thicknesses, and we take the mean values of the $\langle \delta T \rangle$ for the four different thicknesses. The results of this are shown in Figure 10. Different symbols represent the results of the different stellar masses as shown in Figure 6. The size $\Delta\theta$ increases with the stellar mass and the size of HII bubbles. At $z = 10$, Pop III stars show $\langle \delta T \rangle \sim 5 - 12$ mK, while galaxies have $\langle \delta T \rangle \sim 19 - 584$ mK and QSOs have $\langle \delta T \rangle \sim 28 - 196$ mK. In Pop III case, there are absorption spheres comparable to emission ones. Hence the net signal becomes small due to the offset. For the QSO case, the emission spheres are relatively small to the central zero-signal holes, hence the net signal decreases. In addition, the net signal decreases for massive QSOs from the offset between emission and absorption, because the absorption region becomes small due to the limited propagation distance of photons. On the other hand, in the case of galaxies, there are deep extended absorption spheres relative to the central holes and inner emission spheres. Thus, galaxies appear to have much stronger 21 cm signals than the Pop III stars and QSOs. The HII regions around luminous QSOs and massive galaxies can be detected by MWA and LOFAR with ~ 100 hours integration. For low-mass galaxies, SKA or an

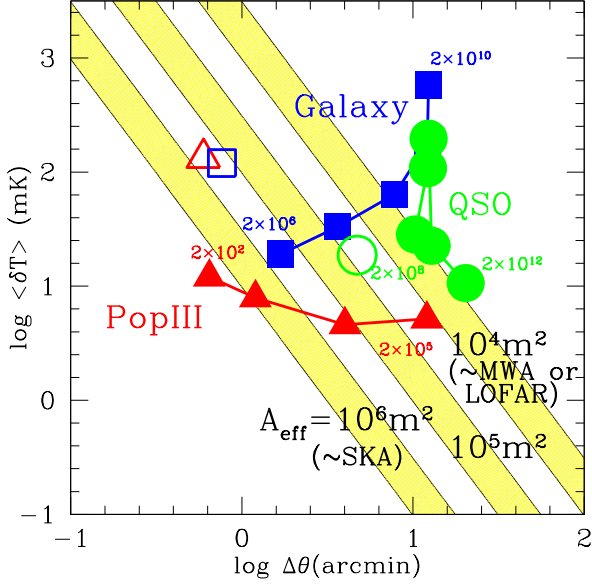


Figure 10. Detectability of the 21 cm signal from Pop III stars, the first galaxies, and the first quasars with upcoming missions MWA, LOFAR, and SKA. The filled symbols represent the δT_b at $z = 10$ with different stellar masses as shown in Figure 6, which is estimated in the spherical top hat beam with size of the distance from the source to the outer edge of $|\delta T_b| = 1$ mK. For each stellar mass, we calculate 2D δT_b maps with widths of $\Delta\nu = 1, 2, 3$ and 4 MHz, and take the mean values of the four slices. With increasing stellar mass, the symbols shift to higher $\Delta\theta$ due to the larger sizes of the HII region and the 21 cm ring. The open symbols are the mean δT_b of the lowest stellar masses for each source at $z = 20$. The yellow shaded regions indicate the sensitivity for $z = 10$ by upcoming facilities with $A_{\text{eff}} = 10^4, 10^5$ and 10^6 m² estimated by equation (16), while its width corresponds to the integration time from 100 to 1000 hours with $\Delta\nu = 1$ MHz.

$A_{\text{eff}} = 10^5$ m² class telescope will be needed to detect the HII regions around them. In the case of Pop III stars with typical mass $M_{\text{star}} \lesssim 1000 M_{\odot}$, however, it appears to be difficult to detect the HII region even with SKA.

At $z = 20$, the $\langle \delta T \rangle$ of a Pop III star with $2 \times 10^2 M_{\odot}$ and a galaxy with $2 \times 10^6 M_{\odot}$ is enhanced by factor $\sim 6-27$ due to the decrease of the sizes of their HII regions and the higher gas density. On the hand, the sensitivity gets lower from $z = 10$ to 20 by factor ~ 20 . Hence, the detectability of Pop III stars and low-mass galaxies does not change significantly. In the case of the QSO with $M_{\text{star}} = 2 \times 10^8 M_{\odot}$, the continuum radiation is significantly diluted in cold neutral region due to the larger HII region. The increase of $S_{\text{ab}}/S_{\text{em}}$ is not large compared to Pop III stars, and hence $\langle \delta T \rangle$ does not change as much. The redshift evolution of the 21 cm structure is also discussed in Section 4

Our results suggest that LOFAR, MWA or SKA may be able to detect the 21 cm signal around galaxies or QSOs, and may be able to distinguish the natures of sources through the difference of emission or absorption and the size. Here, we optimistically assume that the beam size of observations is comparable to the size of the outer emission/absorption shells. In practice, the beam size can be larger than the one used in our models. As a result, the net signal may de-

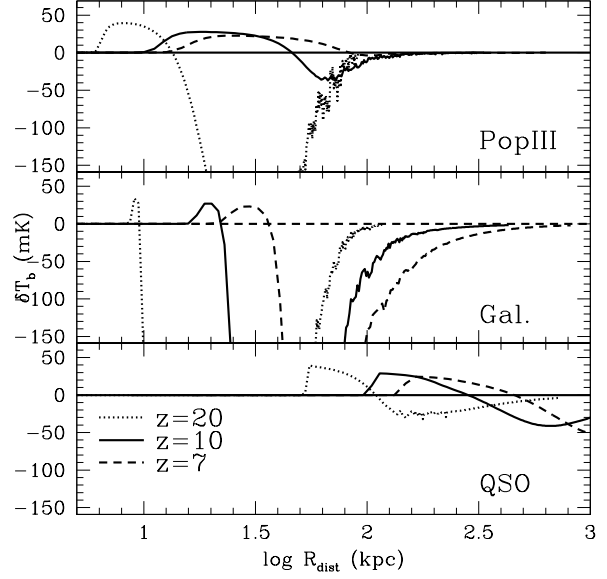


Figure 11. The differential brightness temperature of Pop III stars ($M_{\text{star}} = 10^2 M_{\odot}$), galaxy ($M_{\text{star}} = 10^6 M_{\odot}$) and QSO ($M_{\text{star}} = 10^8 M_{\odot}$) at $z = 7, 10$ and 20. The snapshots at $t_{\text{evo}} = 10^7$ yr.

crease with the beam size. However, the decrease will follow the same gradient of the sensitivity curve $\Delta\theta^{-2}$, hence it may not significantly affect the detectability in the above discussion. In addition, note that we have ignored UV background radiation in this work. If there is UV background radiation and x_{α} becomes ≥ 1 at everywhere, even IGM far from sources will show emission or absorption (e.g., Baek et al. 2009). This leads to a uniform 21 cm signal over the whole sky, and makes the identification of individual sources difficult. For such a case, only high-redshift QSOs can be identified via detection of giant holes in 21 cm sky map (Vonlanthen et al. 2011). In addition, the X-ray background made by black holes and supernovae affects the 21 cm signal by heating the IGM (Furlanetto & Oh 2006; Yajima & Khochfar 2014). The strength of UV and X-ray background depends on the cosmic star formation history and the formation of massive black holes, which are still under the debate. Recent observation of high-redshift galaxies have suggested that the cosmic star formation rate steeply decreases with increasing redshift at $z \gtrsim 8$ (e.g., Oesch et al. 2013). If so, x_{α} is unlikely to be much higher than unity at $z \sim 10$. Therefore, the 21 cm structure around sources at $z \lesssim 20$ should be studied along with formation of galaxies and black holes in a large volume. We will investigate the 21 cm structure's relationship with galaxy formation through cosmological simulation in future work.

4 DISCUSSION

In this work, we focus on the 21 cm signal at $z = 10$. However, the size of the ionizing bubble and the propagation distance of Ly α change at different redshifts. We test the change of δT_b structure at $z = 7$ and 20 with same source properties. Figure 11 shows the δT_b structure with

$t_{\text{evo}} = 10^7$ yr at different redshifts. The size of ionized bubbles decreases with increasing redshift, while the ionizing front becomes closer to the Strömgren radius in the same propagation time. As a result, the expansion rate of the ionizing front is estimated by

$$\frac{R_I'}{R_I} = \left(\frac{1+z'}{1+z} \right)^{-2} \left[\frac{1 - e^{-A(1+z')^3}}{1 - e^{-A(1+z)^3}} \right]^{1/3} \quad (17)$$

where $A = t_{\text{evo}} \alpha_B n_0^{-1}$. Hence, the size ratio of $z = 7$ (20) to $z = 10$ is ~ 1.2 (0.5). For Pop III stars at $z = 20$, there is a deep extended absorption area. With decreasing redshift, the absorption signal becomes shallower, because the distance to the cold-neutral region becomes large, leading to a larger travel time to there. In the case of galaxies, the 21 cm structure is almost the same, however, the absorption area is relatively small at lower redshift, because the HII bubble is bigger and the transition from ionized to neutral becomes more smooth due to the lower density. Note that the QSO at $z = 20$ shows a clear absorption signal, despite the fact that the HII region is much larger than that of Pop III star at $z = 7$ which does not show a clear absorption signal. This is due to the higher Ly α luminosity of the continuum spectrum than the Pop III star.

5 SUMMARY

In this paper, we investigate the redshifted 21 cm signal from different ionizing sources by combining idealized models of the first stars, the first galaxies, and quasars with radiative transfer simulations that include both ionization of neutral hydrogen and resonant scattering of Ly α photons. We find that the 21 cm signal depends significantly on the source SED and stellar mass. The Pop III stars and quasars produce a smooth transition from an ionized and hot state to a neutral and cold one, owing to their hard SED with abundant ionizing photons, in contrast to the sharp transition in galaxies. The HII bubble size is typically ~ 20 kpc for PopIII stars, ~ 100 kpc for galaxies, and ~ 5 Mpc for QSOs. Furthermore, Ly α scattering plays a dominant role in producing the 21 cm signal as it determines the relation between hydrogen spin temperature and gas kinetic temperature. The Ly α photons can produce both emission and absorption region around the small HII bubbles of PopIII stars, extended absorption region around the first galaxies, and extended emission around QSOs.

We predict that future surveys from large radio arrays such as MWA, LOFAR and SKA may be able to detect the 21 cm signals of primordial galaxies and quasars, but not likely Pop III stars due to their small angular diameter.

These results are based on idealized models of the first stars, the first galaxies, and quasars. We will investigate the 21 cm structures in more realistic scenarios including inhomogeneous density, metal enrichment and black hole growth by using cosmological simulations in future works.

ACKNOWLEDGMENTS

Support from NSF grants AST-0965694, AST-1009867 (to YL), and AST-0807075 (to TA) is gratefully acknowledged.

We acknowledge the Research Computing and Cyberinfrastructure unit of Information Technology Services at The Pennsylvania State University for providing computational resources and services that have contributed to the research results reported in this paper (URL: <http://rc.its.psu.edu>). The Institute for Gravitation and the Cosmos is supported by the Eberly College of Science and the Office of the Senior Vice President for Research at the Pennsylvania State University.

REFERENCES

- Abel T., Bryan G. L., Norman M. L., 2002, *Science*, 295, 93
- Alvarez M. A., Pen U.-L., Chang T.-C., 2010, *ApJ*, 723, L17
- Baek S., Di Matteo P., Semelin B., Combes F., Revaz Y., 2009, *A&A*, 495, 389
- Baek S., Semelin B., Di Matteo P., Revaz Y., Combes F., 2010, *A&A*, 523, A4
- Bouwens R. J. et al., 2012, *ApJ*, 752, L5
- Bromm V., Coppi P. S., Larson R. B., 2002, *ApJ*, 564, 23
- Bromm V., Kudritzki R. P., Loeb A., 2001, *ApJ*, 552, 464
- Bromm V., Ferrara A., Coppi P. S., Larson R. B., 2001, *MNRAS*, 328, 969
- Bromm V., Yoshida N., 2011, *ARA&A*, 49, 373
- Cen R., 1992, *ApJS*, 78, 341
- Chen X., Miralda-Escudé J., 2004, *ApJ*, 602, 1
- , 2008, *ApJ*, 684, 18
- Chuzhoy L., Zheng Z., 2007, *ApJ*, 670, 912
- Clark P. C., Glover S. C. O., Smith R. J., Greif T. H., Klessen R. S., Bromm V., 2011, *Science*, 331, 1040
- Datta K. K., Friedrich M. M., Mellema G., Iliev I. T., Shapiro P. R., 2012, *MNRAS*, 424, 762
- Dewdney P. E., Hall P. J., Schilizzi R. T., Lazio T. J. L. W., 2009, *IEEE Proceedings*, 97, 1482
- Di Matteo T., Colberg J., Springel V., Hernquist L., Sijacki D., 2008, *ApJ*, 676, 33
- Di Matteo T., Khandai N., DeGraf C., Feng Y., Croft R. A. C., Lopez J., Springel V., 2012, *ApJ*, 745, L29
- Dijkstra M., Haiman Z., Spaans M., 2006, *ApJ*, 649, 14
- Ellis R. S. et al., 2013, *ApJ*, 763, L7
- Fan X., Carilli C. L., Keating B., 2006a, *ARA&A*, 44, 415
- Fan X. et al., 2006b, *AJ*, 132, 117
- Furlanetto S. R., 2006, *MNRAS*, 371, 867
- Field G. B., 1958, *Proceedings of the IRE*, 46, 240
- Finkelstein S. L., Rhoads J. E., Malhotra S., Grogin N., 2009, *ApJ*, 691, 465
- Fioc M., Rocca V. B., 1997, *A&A*, 326, 950
- Furlanetto S. R. et al., 2009, in *Astronomy*, Vol. 2010, *astro2010: The Astronomy and Astrophysics Decadal Survey*, p. 83
- Furlanetto S. R., Oh S. P., 2006, *ApJ*, 652, 849
- Geil P. M., Wyithe J. S. B., 2008, *MNRAS*, 386, 1683
- Gnedin N. Y., Ostriker J. P., 1997, *ApJ*, 486, 581
- Greif T. H., Bromm V., Clark P. C., Glover S. C. O., Smith R. J., Klessen R. S., Yoshida N., Springel V., 2012, *MNRAS*, 424, 399
- Greif T. H., Glover S. C. O., Bromm V., Klessen R. S., 2010, *ApJ*, 716, 510
- Gunn J. E., Peterson B. A., 1965, *ApJ*, 142, 1633

- Harker G. et al., 2010, MNRAS, 405, 2492
- Heger A., Woosley S. E., 2002, ApJ, 567, 532
- Hirata C. M., 2006, MNRAS, 367, 259
- Hopkins P. F., Richards G. T., Hernquist L., 2007, ApJ, 654, 731
- Iliev I. T., Mellema G., Shapiro P. R., Pen U.-L., Mao Y., Koda J., Ahn K., 2012, MNRAS, 423, 2222
- Johnson J. L., Dalla V. C., Khochfar S., 2013, MNRAS, 428, 1857
- Kashikawa N. et al., 2011, ApJ, 734, 119
- Komatsu E. et al., 2011, ApJS, 192, 18
- Kuhlen M., Madau P., Montgomery R., 2006, ApJ, 637, L1
- Lai K., Huang J.-S., Fazio G., Cowie L. L., Hu E. M., Kakazu Y., 2007, ApJ, 655, 704
- Laor A., Draine B. T., 1993, ApJ, 402, 441
- Laursen P., Razoumov A. O., Sommer-Larsen J., 2009, ApJ, 696, 853
- Li Y. et al., 2007, ApJ, 665, 187
- Liszt H., 2001, A&A, 371, 698
- Loeb A., Barkana R., 2001, ARA&A, 39, 19
- Loeb A., Rybicki G. B., 1999, ApJ, 524, 527
- Lonsdale C. J. et al., 2009, IEEE Proceedings, 97, 1497
- Majumdar S., Bharadwaj S., Choudhury T. R., 2012, MNRAS, 426, 3178
- Marconi A., Hunt L. K., 2003, ApJ, 589, L21
- Marconi A., Risaliti G., Gilli R., Hunt L. K., Maiolino R., Salvati M., 2004, MNRAS, 351, 169
- Maselli A., Ferrara A., Ciardi B., 2003, MNRAS, 345, 379
- McQuinn M., Zahn O., Zaldarriaga M., Hernquist L., Furlanetto S. R., 2006, ApJ, 653, 815
- Mellema G., Iliev I. T., Pen U.-L., Shapiro P. R., 2006, MNRAS, 372, 679
- Mesinger A., Furlanetto S., Cen R., 2011, MNRAS, 411, 955
- Morales M. F., Wyithe J. S. B., 2010, ARA&A, 48, 127
- Mortlock D. J. et al., 2011, Nature, 474, 616
- Nakajima K. et al., 2012, ApJ, 745, 12
- Naoz S., Barkana R., 2008, MNRAS, 385, L63
- Oesch P. A. et al., 2013, ApJ, 773, 75
- Ono Y. et al., 2010, MNRAS, 402, 1580
- Ota K. et al., 2010, PASJ, 62, 1167
- Ouchi M. et al., 2010, ApJ, 723, 869
- Paardekooper J.-P., Khochfar S., Dalla Vecchia C., 2013, MNRAS, 429, L94
- Paciga G. et al., 2011, MNRAS, 413, 1174
- Parsons A. R. et al., 2010, AJ, 139, 1468
- Pawlik A. H., Milosavljević M., Bromm V., 2011, ApJ, 731, 54
- Pawlik A. H., Schaye J., van Scherpenzeel E., 2009, MNRAS, 394, 1812
- Planck Collaboration, 2013, (arXiv:1303.5076)
- Pritchard J. R., Furlanetto S. R., 2006, MNRAS, 367, 1057
- Pritchard J. R., Loeb A., 2012, Reports on Progress in Physics, 75, 086901
- Rix H.-W. et al., 2004, ApJS, 152, 163
- Robertson B. E., Ellis R. S., Dunlop J. S., McLure R. J., Stark D. P., 2010, Nature, 468, 49
- Salpeter E. E., 1955, ApJ, 121, 161
- Semelin B., Combes F., Baek S., 2007, A&A, 474, 365
- Sijacki D., Springel V., Haehnelt M. G., 2009, MNRAS, 400, 100
- Spitzer L., 1978, Physical processes in the interstellar medium, Spitzer, L., ed.
- Tokutani M., Yoshida N., Oh S. P., Sugiyama N., 2009, MNRAS, 395, 777
- Turk M. J., Abel T., O'Shea B., 2009, Science, 325, 601
- Umehura M., Susa H., Hasegawa K., Suwa T., Semelin B., 2012, Prog. Theor. Exp. Phys, 01A306
- Verhamme A., Schaerer D., Maselli A., 2006, A&A, 460, 397
- Volonteri M., Begelman M. C., 2010, MNRAS, 409, 1022
- Vonlanthen P., Semelin B., Baek S., Revaz Y., 2011, A&A, 532, A97
- Willott C. J. et al., 2010a, AJ, 140, 546
- Willott C. J. et al., 2010b, AJ, 139, 906
- Wise J. H., Abel T., 2007, ApJ, 665, 899
- , 2008, ApJ, 685, 40
- Wise J. H., Turk M. J., Abel T., 2008, ApJ, 682, 745
- Wise J. H., Cen R., 2009, ApJ, 693, 984
- Wise J. H., Turk M. J., Norman M. L., Abel T., 2012, ApJ, 745, 50
- Wouthuysen S. A., 1952, AJ, 57, 31
- Wyithe J. S. B., Loeb A., 2007, MNRAS, 375, 1034
- Wyithe J. S. B., Loeb A., Barnes D. G., 2005, ApJ, 634, 715
- Yajima H., Choi J.-H., Nagamine K., 2011, MNRAS, 412, 411
- Yajima H., Li Y., Zhu Q., 2013, ApJ, in press (arXiv:1210.6440)
- Yajima H., Li Y., Zhu Q., Abel T., 2012a, MNRAS, 424, 884
- Yajima H., Li Y., Zhu Q., Abel T., Gronwall C., Ciardullo R., 2012b, (arXiv:1209.5842)
- Yajima H., Khochfar S., 2014, submitted to MNRAS (arXiv:1405.7385)
- Yoshida N., Oh S. P., Kitayama T., Hernquist L., 2007, ApJ, 663, 687
- Yoshida N., Omukai K., Hernquist L., 2008, Science, 321, 669
- Zheng Z., Miralda-Escudé J., 2002, ApJ, 578, 33